Supplementary Information (SI) for

Unexpected anthropogenic emission decreases explain recent atmospheric mercury concentration declines

Aryeh Feinberg[a]*, Noelle E. Selin[a,b], Christine F. Braban[c], Kai-Lan Chang[d,e], Danilo Custódio[f], Daniel A. Jaffe[g,h], Katriina Kyllönen[i], Matthew S. Landis[j], Sarah R. Leeson[c], Winston Luke[k], Koketso M. Molepo[l], Marijana Murovec[m], Michelle G. Nerentorp Mastromonaco[n], Katrine Aspmo Pfaffhuber[o], Julian Rüdiger[p], Guey-Rong Sheu[q], and Vincent L. St.Louis[r]

[a] *Institute for Data, Systems, and Society, Massachusetts Institute of Technology, Cambridge, MA 02139, USA*

[b] *Department of Earth, Atmospheric, and Planetary Sciences, Massachusetts Institute of Technology, Cambridge, MA 02139, USA*

[c] *UK Centre for Ecology & Hydrology (UKCEH), Penicuik, Midlothian EH26 0QB, UK*

[d] *Cooperative Institute for Research in Environmental Sciences, University of Colorado, Boulder, CO 80309-0401, USA*

[e] *NOAA Chemical Sciences Laboratory, Boulder, CO 80305, USA*

[f] *Max-Planck-Institut für Biogeochemie, D-07745 Jena, Germany*

[g] *School of STEM, University of Washington Bothell, Bothell, WA 98011, USA*

[h] *Department of Atmospheric Sciences, University of Washington Seattle, Seattle, WA 98195, USA*

[i] *Finnish Meteorological Institute, Helsinki 00560, Finland*

[j] *United States Environmental Protection Agency, Office of Research and Development, Research Triangle Park, NC 27711, USA*

[k] *NOAA/Air Resources Laboratory, College Park, MD 20740, USA*

[l] *Institute of Coastal Environmental Chemistry, Helmholtz Zentrum Hereon, 21502 Geesthacht, Germany*

[m] *Slovenian Environment Agency, Environment and Nature protection Office, Air Quality Division,1000 Ljubljana, Slovenia*

[n] *IVL Swedish Environmental Research Institute, SE-411 33 Gothenburg, Sweden*

[o] *NILU, 2027 Kjeller, Norway*

[p] *Air Monitoring Network, German Environment Agency, 63225 Langen, Germany*

[q] *Department of Atmospheric Sciences, National Central University, Taoyuan 320, Taiwan*

[r] *Department of Biological Sciences, University of Alberta, Edmonton, AB T6G 2E9, Canada*

*Correspondence to: arifeinberg@gmail.com (A.F.)

This PDF file includes:

Section S1. Observation station information

Table S1. List of sites measuring gaseous elemental mercury (GEM: Hg^0) or total gaseous mercury (TGM) included in this study.

Site code	Location	Latitude	Longitude	Measurement network	IPCC region[a]	Years available	Measured quantity
AL19	Birmingham, USA	33.6	-86.8	AMNet[b]	5	2009–2015	Hg^0
FL96	Pensacola, USA	30.5	-87.4	AMNet[b]	5	2009–2015	Hg^0
GA40	Yorkville, USA	33.9	-85.0	AMNet[b]	5	2009–2015	Hg^0
MD08	Piney Reservoir, USA	39.7	-79.0	AMNet[b]	5	2009–2021	Hg^0
MD98	Beltsville, USA	39.0	-76.8	AMNet[b]	5	2009–2021	Hg^0
MS99	Grand Bay, USA	30.4	-88.4	AMNet[b]	5	2009–2020	Hg^0
NY06	Bronx, USA	40.9	-73.9	AMNet[b]	5	2008–2020	Hg^0
NY20	Huntington Forest, USA	44.0	-74.2	AMNet[b]	5	2009–2021	Hg^0
NY43	Rochester, USA	43.1	-77.5	AMNet[b]	5	2008–2020	Hg^0
OH02	Athens, USA	39.3	-82.1	AMNet[b]	5	2009–2020	Hg^0
OH52	South Bass Island, USA	41.7	-82.8	AMNet[b]	5	2013–2021	Hg^0
OK99	Stilwell, USA	35.8	-94.7	AMNet[b]	4	2009–2015	Hg^0
UT97	Salt Lake City, USA	40.7	-112.0	AMNet[b]	3	2008–2017	Hg^0
VT99	Underhill, USA	44.5	-72.9	AMNet[b]	5	2009–2016	Hg^0
WI07	Horicon Marsh, USA	43.5	-88.6	AMNet[b]	5	2011–2017	Hg^0
MLO	Mauna Loa, USA	19.5	-155.6	AMNet[b]/EPA[c]/NOAA	47	2002–2021	Hg^0
MBA	Mt. Bachelor, USA	44.0	-121.7	GMOS[d]	3	2004–2012	Hg^0 / TGM[*]
ALT	Alert, Canada	82.5	-62.3	ECCC[e]	0	1995–2021	Hg^0 / TGM[†]
BNT	Burnt Island, Canada	45.8	-82.9	ECCC[e]	5	1998–2007	TGM
BRL	Bratt's Lake, Canada	50.2	-104.7	ECCC[e]	2	2001–2013	TGM
EGB	Egbert, Canada	44.2	-79.8	ECCC[e]	5	1996–2018	TGM
KEJ	Kejimkujik, Canada	44.4	-65.2	AMNet[b]/ ECCC[e]	5	1996–2018	Hg^0 / TGM[‡]
LFL	Little Fox Lake, Canada	61.4	-135.6	ECCC[e]	1	2007–2021	TGM
PPT	Point Petre, Canada	43.8	-77.1	ECCC[e]	5	1996–2007	TGM
SAT	Saturna, Canada	48.8	-123.2	ECCC[e]	3	2009–2018	TGM
STA	Huntsman Science Centre, Canada	45.1	-67.1	ECCC[e]	5	1995–2007	TGM
WBZ	St. Anicet, Canada	45.1	-74.3	ECCC[e]	5	1994–2009	TGM
YGW	Kuujuarapik, Canada	55.3	-77.7	ECCC[e]	2	1999–2009	TGM
ELA	Experimental Lakes Area, Canada	49.7	-93.7	IISD[f]	4	2005–2013	Hg^0
AND	Andøya, Norway	69.3	16.0	EMEP[g]	16	2004–2021	Hg^0
AUC	Auchencorth Moss, UK	55.8	-3.2	EMEP[g]	16	2006–2022	Hg^0 / TGM[#]
BIR	Birkenes, Norway	58.4	8.3	EMEP[g]	16	2004–2023	Hg^0 / TGM[§]
BRE	Bredkälen, Sweden	63.9	15.3	EMEP[g]	16	2009–2021	TGM
HAL	Hallahus/Vavihill[h], Sweden	56.0	13.1	EMEP[g]	16	2009–2021	TGM
HYY	Hyytiälä, Finland	61.6	24.0	EMEP[g]	16	2009–2021	TGM
ISK	Iskrba, Slovenia	45.6	14.9	EMEP[g]	17	2009–2021	TGM
LAH	Lahemaa, Estonia	59.5	25.9	EMEP[g]	16	2012–2021	Hg^0
LST	Lista, Norway	58.1	6.6	EMEP[g]	16	1992–2004	TGM
MHD	Mace Head, Ireland	53.3	-9.9	EMEP[g]/GMOS[d]	16	1996–2022	TGM
PAL	Pallas, Finland	68.0	24.4	EMEP[g]/GMOS[d]	16	1996–2021	TGM
RAO	Råö, Sweden	57.4	11.9	EMEP[g]/GMOS[d]	16	2002–2020	TGM
SCA	Schauinsland, Germany	47.9	7.9	EMEP[g]	17	2011–2021	TGM
SCK	Schmücke, Germany	50.7	10.8	EMEP[g]	17	2007–2021	TGM
STN	Station Nord/Villum, Greenland	81.6	-16.6	EMEP[g]	0	2000–2021	TGM
VIR	Virolahti, Finland	60.5	27.7	EMEP[g]	16	2008–2021	TGM
WAL	Waldhof, Germany	52.8	10.8	EMEP[g]	17	2002–2021	TGM
ZEP	Zeppelin, Norway	78.9	11.9	EMEP[g]	46	1996–2022	Hg^0 / TGM[¶]
ZIN	Zingst, Germany	54.4	12.7	EMEP[g]	16	1999–2021	TGM
TW01	Mt. Lulin, Taiwan	23.5	120.9	AMNet[b] / MOENV Taiwan[i]	35	2006–2020	Hg^0
CHE	Cape Hedo, Japan	26.9	128.3	MOEJ[j]	35	2007–2022	Hg^0
OGA	Oga Peninsula, Japan	39.9	139.9	MOEJ[j]	35	2014–2022	Hg^0

[a] IPCC regions are defined with the numbering in Fig. 1, taken from Iturbide et al. (1) [b] Gay et al. (2) [c] Carbone et al. (3)
[d] Sprovieri et al. (4) [e] Cole et al. (5) [f] St. Louis et al. (6) [g] Tørseth et al. (7) [h] Site changed location in 2016, but due to nearby locations (<3 km apart), they are combined in this analysis [i] Nguyen et al. (8) [j] Marumoto et al. (9)
[*] MBA: TGM (2004) and Hg^0 (2005–2012) [†] ALT: TGM (1995–2021) and Hg^0 (2002–2021); analyzed TGM
[‡] KEJ: TGM (1996–2018) and Hg^0 (2009–2018); analyzed TGM [#] AUC: TGM (2006–2013) and Hg^0 (2012–2022)
[§] BIR: TGM (2004–2010) and Hg^0 (2011–2023) [¶] ZEP: TGM (1996–2000) and Hg^0 (2000–2022)

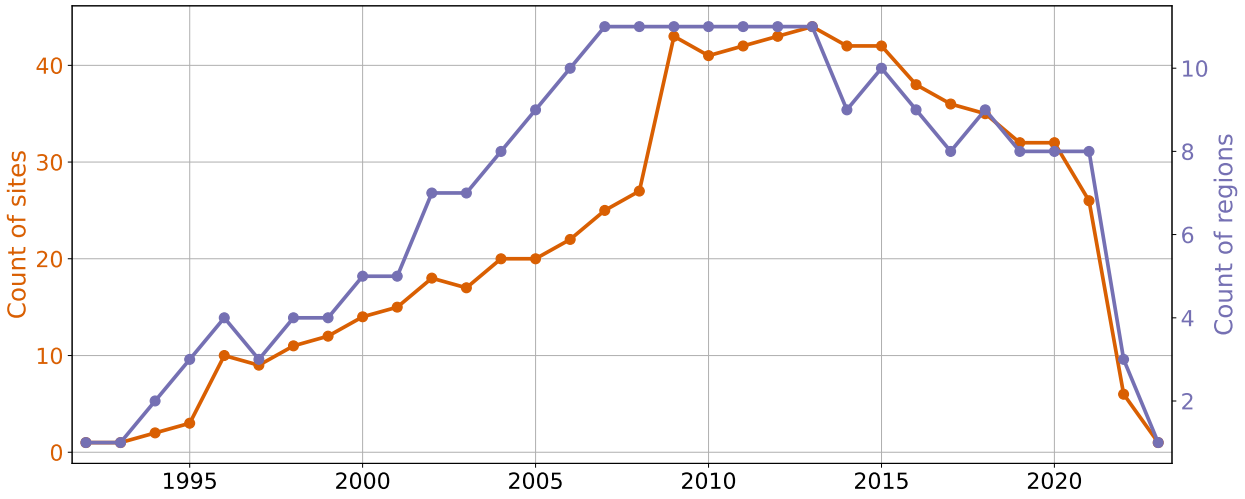

Figure S1. Timeseries showing count of measurement sites included in this study by operation year. The orange curve shows the number of sites measured in each year and the purple curve shows the number of Northern Hemisphere (NH) IPCC regions (Fig. 1) measured in each year. Note that 2022 and 2023 data may still be undergoing quality control procedures by networks and therefore was not yet released at the time of analysis; more data from these years will likely be made available in the future.

Section S2. Trend results by region

Table S2. Tabulated overall regional trends (± 2σ) calculated through linear mixed effects modelling for full available time period of each region.

Region name (number)	Number of sites	Area (10^6 km^2)	Trend (ng m^{-3} yr^{-1})	Time period
Eastern North America (5)	19	5.69	-0.016 ± 0.011	1994–2022
Northern Europe (16)	13	5.00	-0.018 ± 0.004	1992–2023
West & Central Europe (17)	4	3.79	-0.024 ± 0.010	2002–2021
Western North America (3)	3	3.14	-0.035 ± 0.025	2004–2018
Central North America (4)	2	2.93	-0.035 ± 0.007	2005–2015
Northeastern North America (2)	2	7.66	-0.032 ± 0.009	1999–2013
Greenland/Iceland (0)	2	4.77	-0.015 ± 0.003	1995–2021
East Asia (35)	3	9.46	-0.023 ± 0.005	2006–2022
North Pacific Ocean (47)	1	51.61	-0.010 ± 0.011	2002–2021
Northwestern North America (1)	1	7.51	0.007 ± 0.003	2007–2021
Arctic Ocean (1)	1	6.35	-0.007 ± 0.002	1996–2022
Northern Hemisphere (NH) area-weighted average	**51**		**-0.011 ± 0.006**	**2005–2020**

Section S3. Sensitivity of trends to statistical approach

Section S3.1 Modelled differences between site, surface, and troposphere NH trends

We used the five GEOS-Chem simulations to test different approaches for calculating overall trends in NH Hg^0 (Fig. S2). We calculated annual averages of the model results over the entire NH troposphere (orange lines), representative of the NH tropospheric box in the 3-box model simulations. We compared this to simulated NH surface Hg^0 concentrations (purple lines), which is the quantity that can actually be measured by surface observation stations. The calculated 2005–2020 trends in surface Hg^0 agree within 0.0007 ng m^{-3} yr^{-1} of tropospheric Hg^0 trends for all simulations except DEC_ANT_NH, where surface declines are faster than tropospheric declines by 0.0015 ng m^{-3} yr^{-1}. This can be explained by enhanced dilution of the negative emissions trends when considering the whole troposphere versus the surface level. To approximate the real situation where only a small fraction of the NH surface is measured, we averaged only the model grid cells that contain the 51 observation sites (magenta line in Fig. S2). This approach leads to biases of up to 0.0044 ng m^{-3} yr^{-1} due to the uneven distribution of observation stations (Fig. 1) throughout the NH, with some regions covered more than others and other regions having no observations. This bias can be reduced to below 0.0006 ng m^{-3} yr^{-1} by first averaging by IPCC region the grid cells that correspond to observation sites (Fig. 1) and then calculating an area-weighted average for the NH (green line), similar to what was done for the observation analysis in the main manuscript (Fig. 2). Therefore, it is best to use the approach of area-weighted site averages when limited observation stations are available, leading to good agreement with the surface trends in Hg^0. We expanded the observed trend uncertainty in Figs. 3A and B upwards by 0.0021 ng m^{-3} yr^{-1} (max error between area-weighted and tropospheric trends, DEC_ANT_NH), due to the potential overestimate of NH tropospheric trends by only having surface observations (Fig. S2).

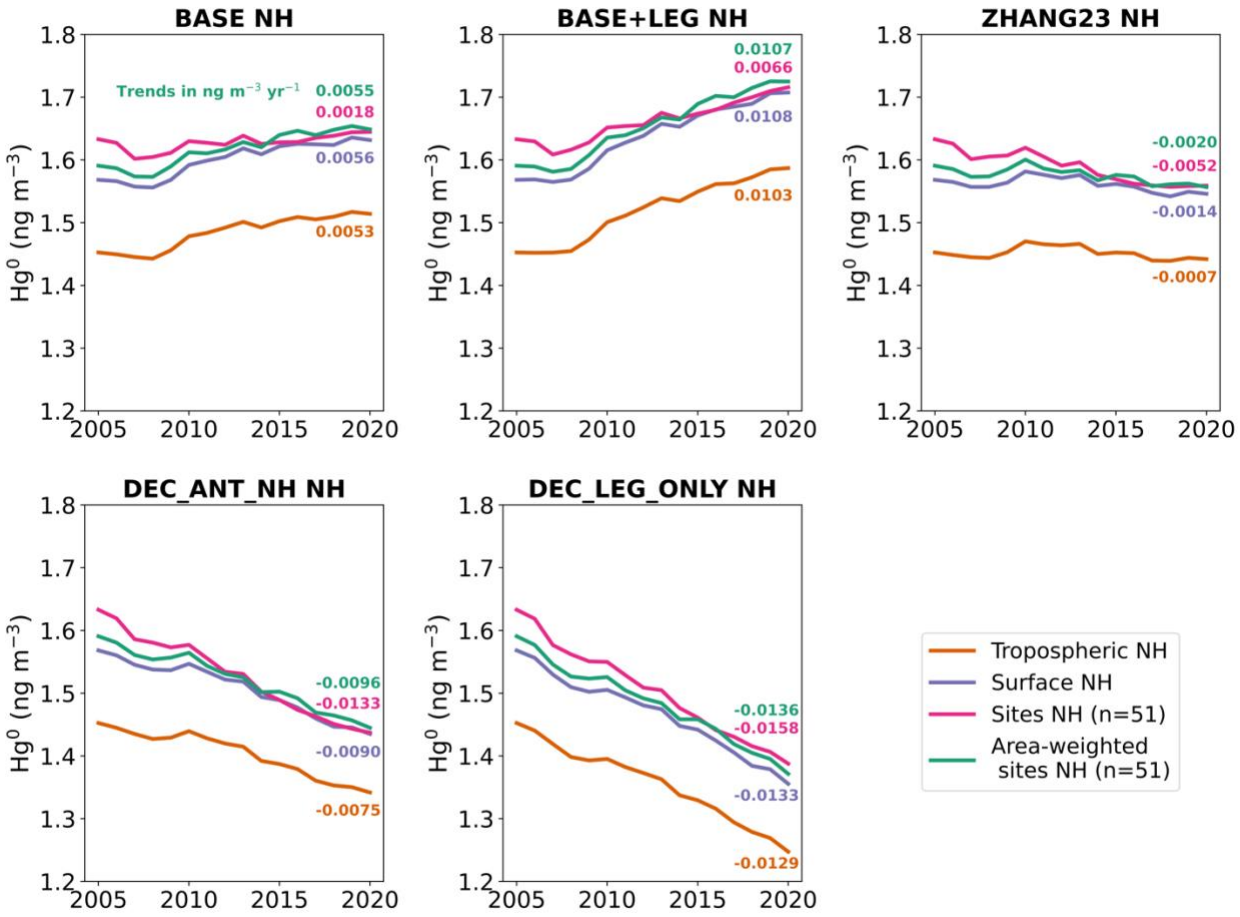

Figure S2. Different methods of calculating hemispheric average trends applied to GEOS-Chem simulated Hg^0. We compared annual mean simulated timeseries of: 1) NH tropospheric averages, 2) NH surface averages, 3) averaging model grid cells where observation sites are located, and 4) area-weighted averaging of regional averages of model grid cells where observation sites are located. Linear regression trends over 2005–2020 are listed in units of ng m^{-3} yr^{-1}.

Section S3.2 Aggregation of observation stations into overall NH annual averages using "bucket" method

Previous studies (e.g., 10) have calculated overall timeseries for regions by averaging all available stations for each specific year ("bucket" method). Biases can arise in this approach from multiple sources of error: 1) sites have individual offsets and trends due to measurement method differences or specific local sources, leading to biases in a "bucket" average because sites do not all cover the same time period; 2) sites are unevenly distributed, with certain regions over- or under-represented; and 3) certain months can be missing in a specific year, which due to the strong seasonality of Hg^0 can bias the annual mean. We aimed to address the drawbacks of the "bucket" approach by explicitly modeling offsets between sites using linear mixed effects models, deseasonalizing monthly means from all observations, and aggregating results by IPCC regions before calculating area-weighted averages. To compare our methods with approaches applied in previous papers, we use the bucket approach to calculate 2005–2020 trends in Eastern North America (19 sites), Northern Europe (13 sites), and the NH (51 sites) (Fig. S3) in a sensitivity test. Overall, the derived trends are similar for the NH between our approach (-0.011 ± 0.006 ng m^{-3} yr^{-1}) and the "bucket" approach (-0.015 ng m^{-3} yr^{-1}). Issues with the bucket method were observed for periods when less sites are available (e.g., before the year 2000 in Fig. S3), which show high variability due to differences in the number and characteristics of averaged sites for each year.

Therefore, we recommend that caution be exercised with such an approach, as the derived aggregated timeseries may be misleading and could be misinterpreted as real variability rather than changes in site availability.

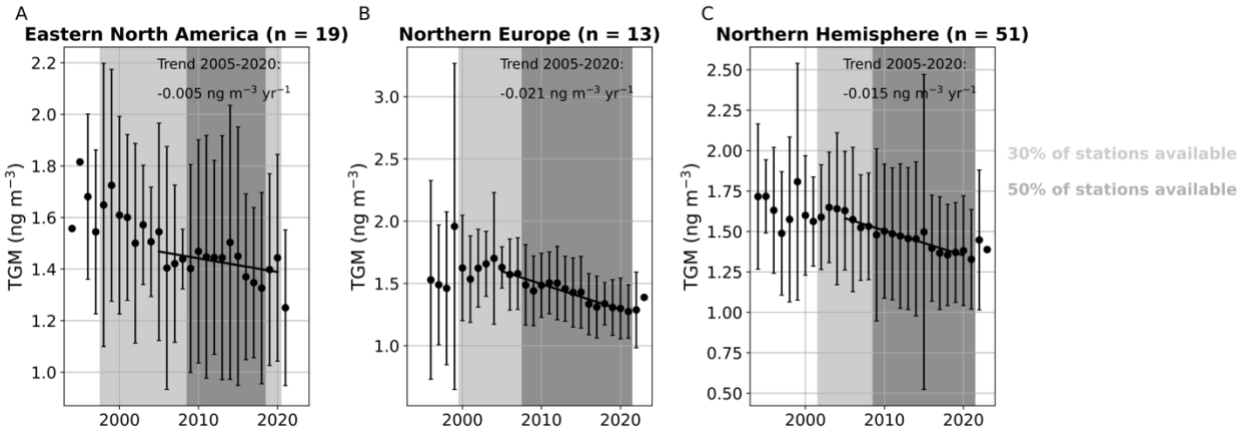

Figure S3. "Bucket" method trends calculated by averaging all available station data (not deseasonalized) for each year for Eastern North America (*A*), Northern Europe (*B*), and the overall Northern Hemisphere (*C*). Error bars show the 2σ variation in station averages. Shading shows the years where at least 30% (light gray) and 50% of the stations (dark gray) are available. Linear regression trends are calculated over 2005–2020 and listed on the plot.

Section S3.3 Using Generalized Additive Models (GAM) to aggregate multisite data

To test the robustness of our regional trend results to other approaches, we applied the approach of Chang et al. (11) to use Generalized Additive Models (GAM) to aggregate multisite data into an overall trend. In this regression-based approach, we modeled the deseasonalized Hg^0 monthly mean values at multiple sites as a function of site (s) and time (t):

$$\text{obs}(s,t) = \text{regional trend}(t) + \text{regional seasonality}(t) + \text{site offset}(s) + \text{site-specific trend}(s,t) + \text{site-specific seasonality}(s,t) + \text{AR}(1)\ \text{error} \quad \text{(Eq. S1)}$$

The GAM approach fits smooth functions of the predictor variables, which include time, month-of-year (for seasonality), and the categorical site ID (for site-specific terms). We used the implementation of GAM in the R package mgcv (12) and calculated fits using the restricted maximum likelihood (REML) method to avoid overfitting.

The GAM method is not suitable when only a few sites are available within a region (13), so in the main manuscript we focused on linear mixed effect models of regional trends. For the GAM analysis here, we investigated the two regions with more than 10 sites (Eastern North America and Northern Europe). GAM helped to identify nonlinearities in the overall regional trend, for example, a deceleration in the Eastern North America Hg^0 decline occurred after ~2009. A previous study has suggested a deceleration in Hg^0 trends in North America around 2008, although different statistical methods were applied on a smaller set of stations (14). We calculated the 2005–2020 linear trend obtained from the GAM curves for Eastern North America (-0.011 ng m^{-3} yr^{-1}) and Northern Europe (-0.019 ng m^{-3} yr^{-1}). Since both of these trends are within the error of the results obtained for linear mixed effects modeling (Eastern North America: -0.016 ± 0.011 ng m^{-3} yr^{-1}; Northern Europe: -0.018 ± 0.004 ng m^{-3} yr^{-1}), we conclude that the derived regional declines are relatively robust to the choice of statistical approach.

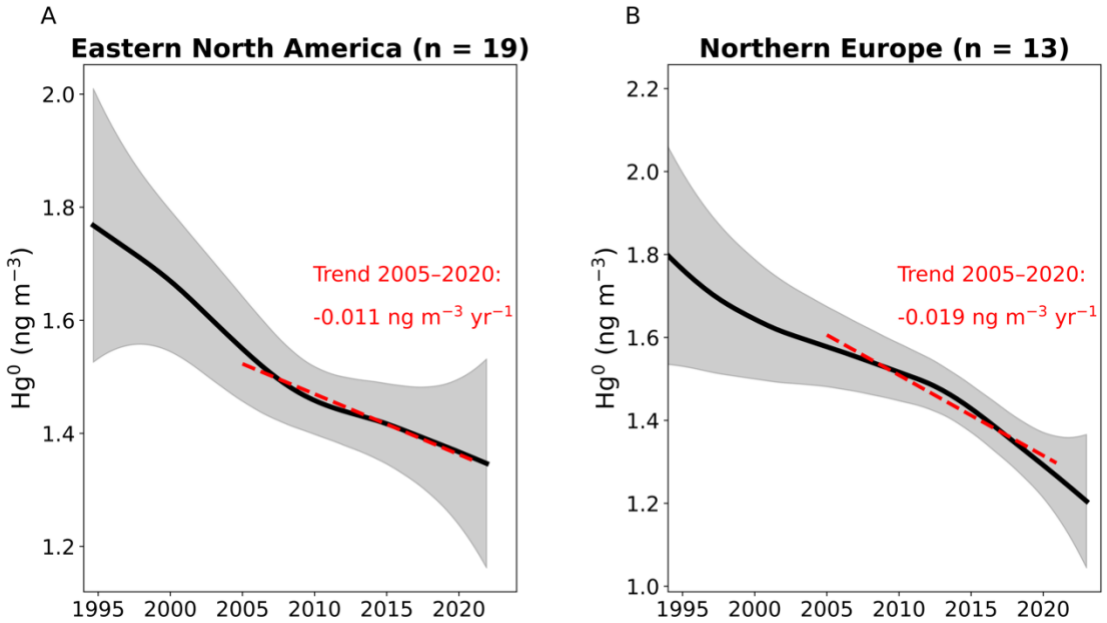

Figure S4. Generalized additive model (GAM) regional trends for multisite deseasonalized total gaseous mercury (Hg^0) data in Eastern North America (*A*) and Northern Europe (*B*). The GAM mean estimate is shown as a black line, with shaded grey areas showing ± 2 standard errors in the GAM estimate. Linear regression trends (red dashed lines) were calculated over the 2005–2020 period from the regional nonlinear GAM curve.

Section S3.4 Restricting the analysis to site data between 2005 and 2020

In the main manuscript (Fig. 2), we use the full set of available data between 1992 and 2022 to calculate linear mixed effects model trends for each region, which are then area-weighted to calculate an average 2005–2020 trend for the Northern Hemisphere (NH). We use the full extent of data to maximize the available information in the calculation of long-term Hg^0 trends. Here, we repeat the analysis but only use data between 2005 and 2020 to calculate the trend, removing all earlier and later data from the analysis. The results are summarized in Fig. S5 and Table S3, which can be compared to Fig. 2 and Table S2. Overall, the regional trends calculated with both datasets are overlapping in their error ranges, with the exception of the Arctic Ocean region (2005–2020: -0.014 ± 0.004 ng m^{-3} yr^{-1}; 1996–2022: -0.007 ± 0.002 ng m^{-3} yr^{-1}). The area-weighted NH average trend in the 2005–2020 calculation is -0.015 ± 0.006 ng m^{-3} yr^{-1}, slightly more negative but overlapping with the trend calculated in the main paper (-0.011 ± 0.006 ng m^{-3} yr^{-1}). Overall, our conclusions remain the same that the NH Hg^0 concentrations are declining between 2005 and 2020 and would be difficult to reconcile with increasing NH anthropogenic emissions.

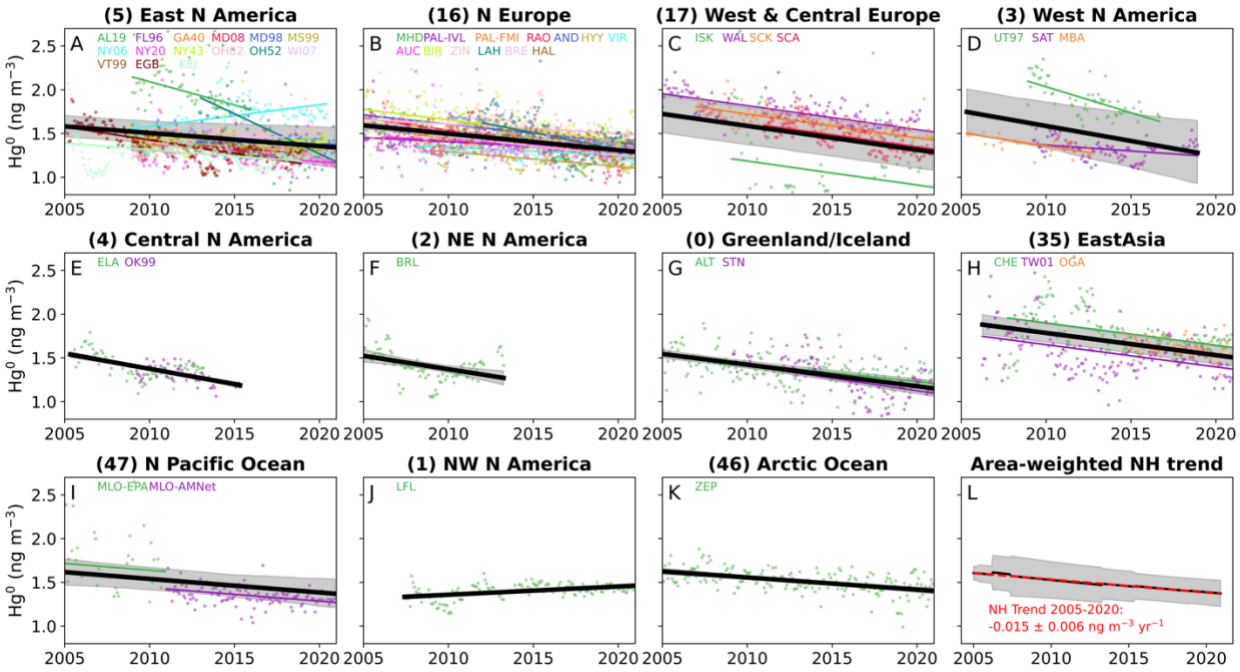

Figure S5. Similar to Fig. 2 but only for the period of 2005–2020, trends in observed gaseous elemental mercury (Hg^0) aggregated by the regions (*A*–*K*) in Fig. 1 (labelled by region number). Trends are calculated with linear mixed effects modeling, with overall regional trends shown in black and shading shows the 5th to 95th percentile range. Individual site deseasonalized monthly means are shown as colored points and individual regressions as colored lines. The overall Northern Hemisphere (NH) trend (*L*) is calculated by taking the area-weighted average of regional trends, with the shading showing the 2σ averaging error. The red dashed curve in *L* is the linear regression trend for 2005–2020, with trend error representing 2σ error from resampling regional trends within their error bounds.

Table S3. Tabulated overall regional trends (± 2σ) calculated through linear mixed effects modelling after restricting site data to 2005–2020 period only. See Table S2 for trends calculated using all data.

Region name (number)	Number of sites	Area (10^6 km^2)	Trend (ng m^{-3} yr^{-1})	Time period
Eastern North America (5)	15	5.69	-0.015 ± 0.015	2005–2020
Northern Europe (16)	12	5.00	-0.019 ± 0.006	2005–2020
West & Central Europe (17)	4	3.79	-0.027 ± 0.005	2005–2020
Western North America (3)	3	3.14	-0.034 ± 0.025	2005–2018
Central North America (4)	2	2.93	-0.035 ± 0.007	2005–2015
Northeastern North America (2)	1	7.66	-0.031 ± 0.016	2005–2013
Greenland/Iceland (0)	2	4.77	-0.025 ± 0.008	2005–2020
East Asia (35)	3	9.46	-0.025 ± 0.006	2006–2020
North Pacific Ocean (47)	1	51.61	-0.015 ± 0.011	2005–2020
Northwestern North America (1)	1	7.51	0.009 ± 0.003	2007–2020
Arctic Ocean (1)	1	6.35	-0.014 ± 0.004	2005–2020
Northern Hemisphere (NH) area-weighted average	**45**		**-0.015 ± 0.006**	**2005–2020**

Section S4. Differences between Hg^0 and TGM measurements

Atmospheric Hg is measured in three operationally-defined fractions: gaseous elemental mercury (GEM, Hg^0), gaseous oxidized mercury (GOM, Hg^{II}), and particulate-bound mercury (PBM, Hg^P). Total gaseous mercury (TGM) refers to the sum of Hg^0 and GOM. Past studies have identified several issues related to the collection of GOM in Tekran instruments, which leads to a low bias of these measurements that can vary over space and time (15–17). For this reason, we do not analyze GOM measurements and focus our analysis on Hg^0 . Previous trend analyses have combined measurements of Hg^0 and TGM, assuming that Hg^0 is the dominant (>98%) fraction of TGM (10, 18, 19). This is supported by analytical studies showing that available TGM measurements from networks do not pick up all GOM, and thus represent a fraction between Hg^0 and true TGM (20). Several measurement networks have also suggested that reported TGM measurements largely represent Hg^0 concentrations (Environment and Climate Change Canada measurement description; GMOS: Sprovieri et al. (4)). Therefore, in the main manuscript, we assume that available TGM and Hg^0 measurements are synonymous and use a combined dataset of these two quantities.

To test this assumption, we conducted a sensitivity test analyzing trends from only sites where Hg^0 data was reported from Tekran or Lumex instruments, removing all TGM data from the analysis. For sites where both Hg^0 and TGM data are available (Table S1), we analyzed only the Hg^0 data for this sensitivity test. The results of this sensitivity test analyzing only Hg^0 are shown in Fig. S6, analogous to Fig. 2 in the main manuscript using the full TGM & Hg^0 dataset. For all regions where TGM measurements were removed, the trend estimates resulting from using only Hg^0 data overlap with our main manuscript analysis. No clear patterns are observed in the differences between the GEM-only and all data trends,

meaning that any differences are probably driven by differences in the data availability and studied time period. The trend estimates are:

East North America (Fig. S6A) – GEM-only: -0.014 ± 0.016 ng m^{-3} yr^{-1}, all data: -0.016 ± 0.011 ng m^{-3} yr^{-1}
Northern Europe (Fig. S6B) – GEM-only: -0.019 ± 0.007 ng m^{-3} yr^{-1}, all data: -0.018 ± 0.004 ng m^{-3} yr^{-1}
West North America (Fig. S6C) – GEM-only: -0.048 ± 0.026 ng m^{-3} yr^{-1}, all data: -0.035 ± 0.025 ng m^{-3} yr^{-1}
Greenland/Iceland (Fig. S6E) – GEM-only: -0.011 ± 0.004 ng m^{-3} yr^{-1}, all data: -0.015 ± 0.003 ng m^{-3} yr^{-1}
Arctic Ocean (Fig. S6H) – GEM-only: -0.007 ± 0.002 ng m^{-3} yr^{-1}, all data: -0.007 ± 0.002 ng m^{-3} yr^{-1}

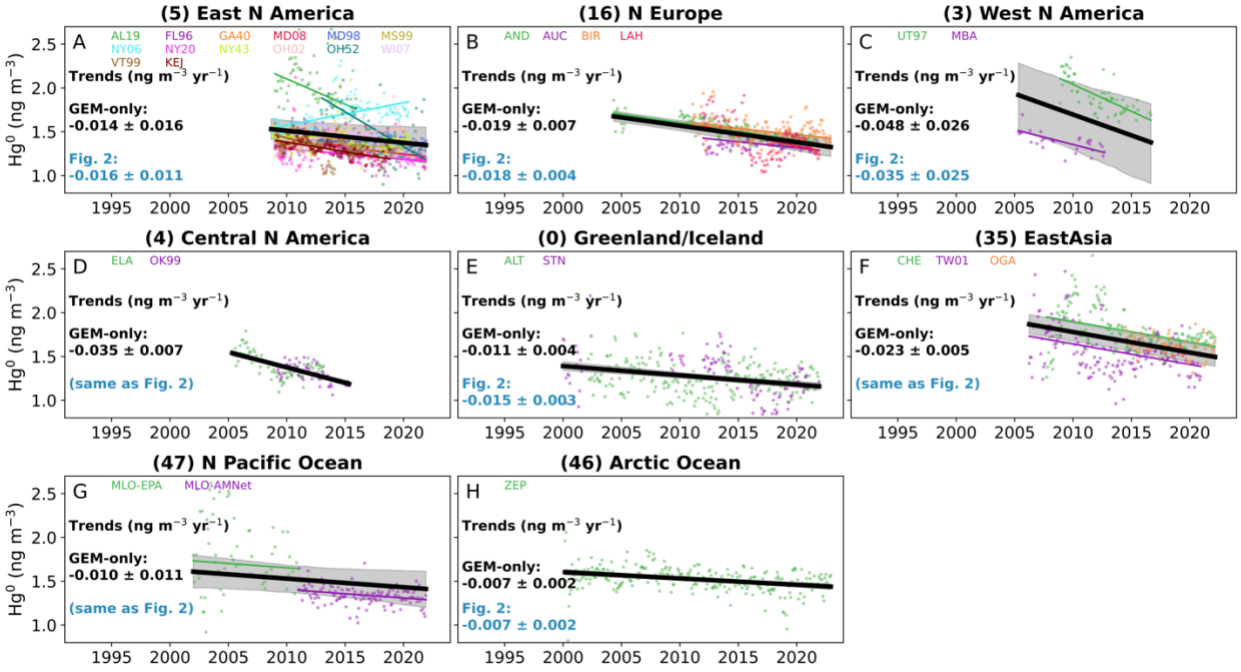

Figure S6. Similar to Fig. 2 but showing only data from Hg^0 measurements (removing all TGM measurements from the dataset). Trends in observed gaseous elemental mercury (GEM: Hg^0) are aggregated by the regions (A–H) in Fig. 1 (labelled by region number). Trends are calculated with linear mixed effects modeling, with overall regional trends shown in black and shading shows the 5th to 95th percentile range. Listed in black are determined regional trend values from the GEM-only analysis with 2σ errors, while in blue are the trends from the full analysis, including TGM measurements. Three regions only have GEM data and are thus identical to Fig. 2: Central North America, East Asia, and North Pacific Ocean. Due to removal of TGM stations, no data is available from the regions: West & Central Europe, Northeastern North America, and Northwestern North America.

All other regions either do not have any sites with Hg^0 measurements (and thus cannot be evaluated), or have no sites with TGM measurements (and thus are unchanged from the main manuscript analysis). Given the overlapping trend estimates between these two analyses, we conclude that the use of both TGM and Hg^0 data does not impact the estimates of the overall regional trends. As well, all trend estimates using only Hg^0 data also show negative trends and thus support the conclusions in the main manuscript.

Our assumption (applied by previous Hg trend studies as well) that TGM and Hg^0 measurements can be combined is supported by this sensitivity test where TGM is fully removed from the trend analysis. We

therefore chose to keep the analysis using both TGM and Hg^0 data in the main manuscript as more locations and time periods are covered.

Section S5. Calculating EAME equations from the GBC box model and perturbation analysis

We followed the approach of Selin (21) to calculate parameters from the EAME equation (Eq. 2) using pulse simulations in the Hg Global Biogeochemical Box model (GBC) (22, 23). We introduced an atmospheric Hg pulse of 100 Mg in the year 2010 and monitored the evolution of legacy re-emissions for 100 years, until 2110 (Fig. S7). The two-term exponential model fits the behaviour of the box model very well (R^2~0.99) on the 100-year time period of the simulation. This fitting reduces the ~40 parameters of the GBC model to 4 understandable parameters, as well as reducing the computation time for legacy re-emissions. We performed a similar experiment by modeling the release of a riverine pulse, and evaluated changes to legacy re-emissions. This equation will differ from the atmospheric pulse, as different timescales are involved (river transport *versus* deposition to oceans) and only a fraction of the riverine pulse will reach the open ocean and not be buried on the coastal shelf.

To estimate a reasonable range in the legacy re-emission pulse parameters (Eq. 2), we performed 1000 parameter perturbation simulations in the GBC model. The 40 relevant parameters that we varied are 35 rate coefficients, 3 parameters for the designation of deposition into soil pools, 1 parameter for geogenic emissions, and 1 parameter for the fraction of riverine particulate Hg reaching the open ocean. These parameters were perturbed simultaneously by factors varying between 0.5 and 2, with Latin Hypercube sampling (24) used to ensure that the parameter space is better explored. For each of the 1000 experiments, we calculated the legacy re-emission pulse parameters (Eq. 2) and selected the 5th–95th percentile of each parameter as the range for simulations in the 3-box atmospheric model (Table S4). The 1000 experiments were conducted twice, once for atmospheric pulses and once for riverine pulses. The code for conducting sensitivity experiments in the GBC model is available here: https://github.com/arifein/gbc-boxmodel-sensitivity.

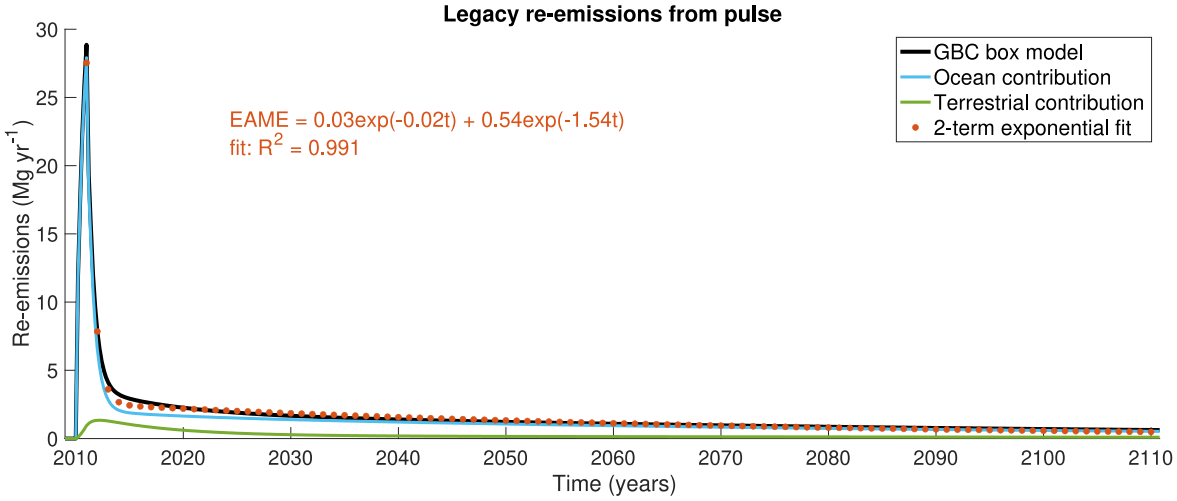

Figure S7. Example of fitting the GBC model pulse experiment to Eq. 2. The contribution of ocean and terrestrial legacy re-emissions to the total are shown as blue and green lines.

Section S6. 3-box atmospheric model parameter variations

The bounds for the 19 parameters that were varied in the 2 × 10^5 simulations, along with their justifications, are listed in Table S4. We sampled the fraction of Hg emitted in the short timescale (f_{short}) and the total re-emissions (E_{total}) instead of directly sampling coefficients a_1 and a_2 in Eq. 2. This is less

likely to lead to unrealistic combinations of the *a* coefficients and the *b* lifetimes. Integrating Eq. 2 between time 0 and infinity yields an equation for E_{total}:

$$E_{\text{total}} = a_1 b_1 + a_2 b_2 \quad \text{(Eq. S2)}$$

The fraction of Hg emitted in the short timescale is equal to:

$$f_{\text{short}} = \frac{a_1 b_1}{a_1 b_1 + a_2 b_2} = \frac{a_1 b_1}{E_{\text{total}}} \quad \text{(Eq. S3)}$$

We calculated the *a* coefficients from the sampled variables (b_1, b_2, f_{short}, E_{total}) using Eq. S4 and Eq. S5:

$$a_1 = \frac{E_{\text{total}}\, f_{\text{short}}}{b_1} \quad \text{(Eq. S4)}$$

$$a_2 = \frac{E_{\text{total}}\, (1 - f_{\text{short}})}{b_2} \quad \text{(Eq. S5)}$$

Table S4. Bounds of parameters varied for the 2005–2020 simulations in the 3-box atmospheric model.

Parameter	Min	Max	Units	Comment/References
Atmospheric Hg lifetime	3	8	months	Horowitz et al. (25); Parrella et al. (26); Zhang et al. (27)
Error in 1970 emissions and releases	-20	+40	%	Error range suggested for 2000, 2010, 2015 emissions in Streets et al. (28)
Error in 1980 emissions and releases	-20	+40	%	Error range suggested for 2000, 2010, 2015 emissions in Streets et al. (28)
Error in 1990 emissions and releases	-20	+40	%	Error range suggested for 2000, 2010, 2015 emissions in Streets et al. (28)
Error in 2000 emissions and releases	-20	+40	%	Error range suggested for 2000, 2010, 2015 emissions in Streets et al. (28)
Error in 2010 emissions and releases	-20	+40	%	Error range suggested for 2000, 2010, 2015 emissions in Streets et al. (28)
Legacy short lifetime (b_1) (atmospheric pulse)	5.7	14.6	months	Based on perturbation analysis of Amos et al. (22, 23) GBC model (Section S5)
Legacy long lifetime (b_2) (atmospheric pulse)	28.6	96.9	years	Based on perturbation analysis of Amos et al. (22, 23) GBC model (Section S5)
Legacy fraction emitted in short timescale (atmospheric pulse)	7	31	%	Based on perturbation analysis of Amos et al. (22, 23) GBC model (Section S5)
Total re-emissions from initial pulse (atmospheric pulse)	79	379	%	Based on perturbation analysis of Amos et al. (22, 23) GBC model (Section S5)
Legacy short lifetime (b_1) (riverine pulse)	1.6	9.5	months	Based on perturbation analysis of Amos et al. (22, 23) GBC model (Section S5)
Legacy long lifetime (b_2) (riverine pulse)	1	116.9	years	Based on perturbation analysis of Amos et al. (22, 23) GBC model (Section S5)
Legacy fraction emitted in short timescale (riverine pulse)	5	55	%	Based on perturbation analysis of Amos et al. (22, 23) GBC model (Section S5)
Total re-emissions from initial pulse (riverine pulse)	2	160	%	Based on perturbation analysis of Amos et al. (22, 23) GBC model (Section S5)
Difference in percent Hg^0 emitted from anthropogenic sources between 2020 and 2005	-20	20	%	The speciation of emissions in longest available inventory (29) varied by 15% (from 60% Hg^0 in 1970 to 75% Hg^0 in 2010)
Anthropogenic emissions trend in Northern Hemisphere (NH)	-70	70	Mg yr^{-2}	Covers wide range without 2020 emissions becoming negative
Anthropogenic emissions trend in Southern Hemisphere (SH)	-10	10	Mg yr^{-2}	Covers wide range without 2020 emissions becoming negative
Deviation of releases trend from emissions trend in NH	-80	80	Mg yr^{-2}	For example, if NH emissions trend is 30 Mg yr^{-2}, the NH releases trend ranges between -21 and 139 Mg yr^{-2} *
Deviation of releases trend from emissions trend in NH	-35	35	Mg yr^{-2}	For example, if SH emissions trend is -10 Mg yr^{-2}, the SH releases trend ranges between -45 and 25 Mg yr^{-2} †

* In the NH, decadal release trends in Streets et al. (30) are 1.97 × emissions trends ± 80

† In the SH, decadal release trends in Streets et al. (30) are 1.03 × emissions trends ± 35

Fig. S8 visualizes the results of the box model simulations by comparing inputted trends in NH emissions with simulated trends in NH Hg^0 over 2005–2020. Fig. S8A displays the relationship between total NH emissions trends (anthropogenic + legacy) and the Hg^0 trend. The NH total emissions trends that would be compatible with the observed Hg^0 trends (grey range in Fig. S8A) ranges from -15 Mg yr^{-2} to more than -80 Mg yr^{-2}. The relationship between the total emissions trends and the Hg^0 trend crosses close to the origin, meaning that with a zero total emissions trend the simulated median Hg^0 trend is negligible. However, in the case of the anthropogenic emissions trend plot (Fig. S8B), a zero trend in NH anthropogenic emissions will still lead to a positive Hg^0 trend due to increasing legacy emissions (31). The NH anthropogenic emissions trend must be below -8 Mg yr^{-2} in order for the NH Hg^0 trend to be negative. Another aspect of Fig. S8 is that relationship between NH Hg^0 trends and anthropogenic emissions trends is associated with larger uncertainties (Fig. S8B) than that of total emissions (Fig. S8A), as evidenced by the larger red error bars in Fig. S8B. The relationship between total NH emissions trends and the NH Hg^0 concentration trend (Fig. S8A) is mainly affected by uncertainties in the atmospheric Hg lifetime, SH emissions, and speciation trends. However, the relationship of anthropogenic NH emissions with Hg^0 concentrations is affected by the uncertain response of legacy emissions to anthropogenic inputs and the trends in releases to water and land that would accompany anthropogenic emissions trends for 2005–2020, leading to larger error bars.

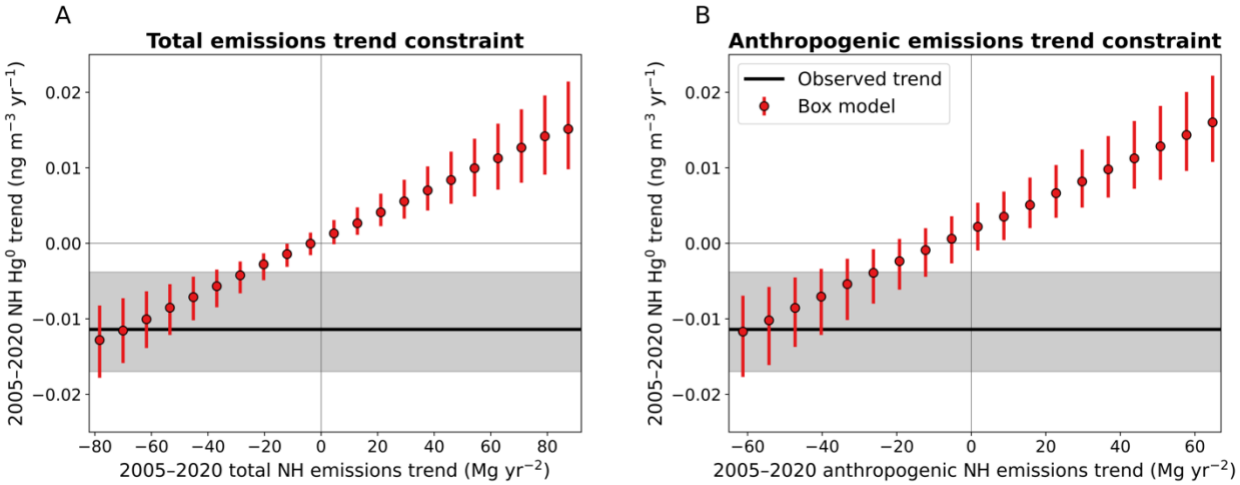

Figure S8. (*A*) Relationship between NH Hg^0 trends and the trends in total NH emissions. The 10^5 box model simulations are summarized in the red points (median) and error bars (5^{th} to 95^{th} percentile). Observed NH TGM trends are shown in the horizontal black line, with the associated error shaded. The overlap between grey shading and red error bars represents the parameter space where the model is compatible with observed trends. (*B*) Relationship between NH Hg^0 trends and trends in anthropogenic NH emissions. Fig. 3A in the main manuscript represents a 1-D representation of these curves for selected values of the anthropogenic NH emissions trend.

The relationships between NH Hg re-emissions trends (2005–2020) and anthropogenic emissions and releases parameters in the 3-box model results are plotted in Fig. S9. We have used Fig. S9F in the main paper to relate the trend in NH anthropogenic emissions from the GEOS-Chem scenarios with the expected NH trend in legacy re-emissions. This relationship was used to identify potential trends in legacy emissions resulting from anthropogenic emissions trends, which can then be incorporated in the GEOS-Chem simulations by scaling ocean Hg^0 concentrations.

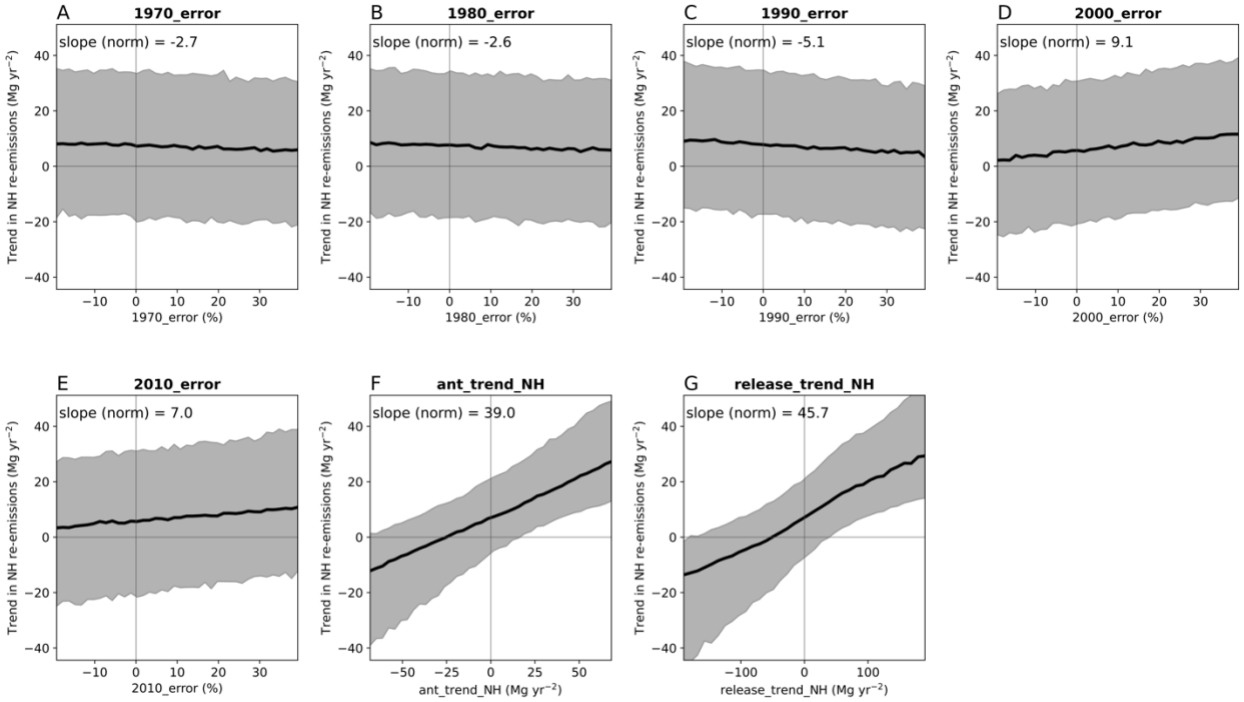

Figure S9. The relationships between Northern Hemisphere (NH) Hg re-emissions trends (2005–2020) and anthropogenic emissions and releases parameters. Plots show the relationship for (*A*) the error in emissions and releases for 1970 in the Streets et al. (30) inventory; (*B*) the error in emissions and releases for 1980; (*C*) the error in emissions and releases for 1990; (*D*) the error in emissions and releases for 2000; (*E*) the error in emissions and releases for 2010; (*F*) the trend in anthropogenic NH emissions for 2005–2020; (*G*) the trend in anthropogenic NH releases for 2005–2020. Black lines show median responses and the shaded area shows the 90% confidence interval (5^{th} to 95^{th} percentile). The slope (normalized to the range of the x-axis parameter) is listed on the plot to illustrate the relative importance of a parameter.

Section S7. Description of GEOS-Chem simulations

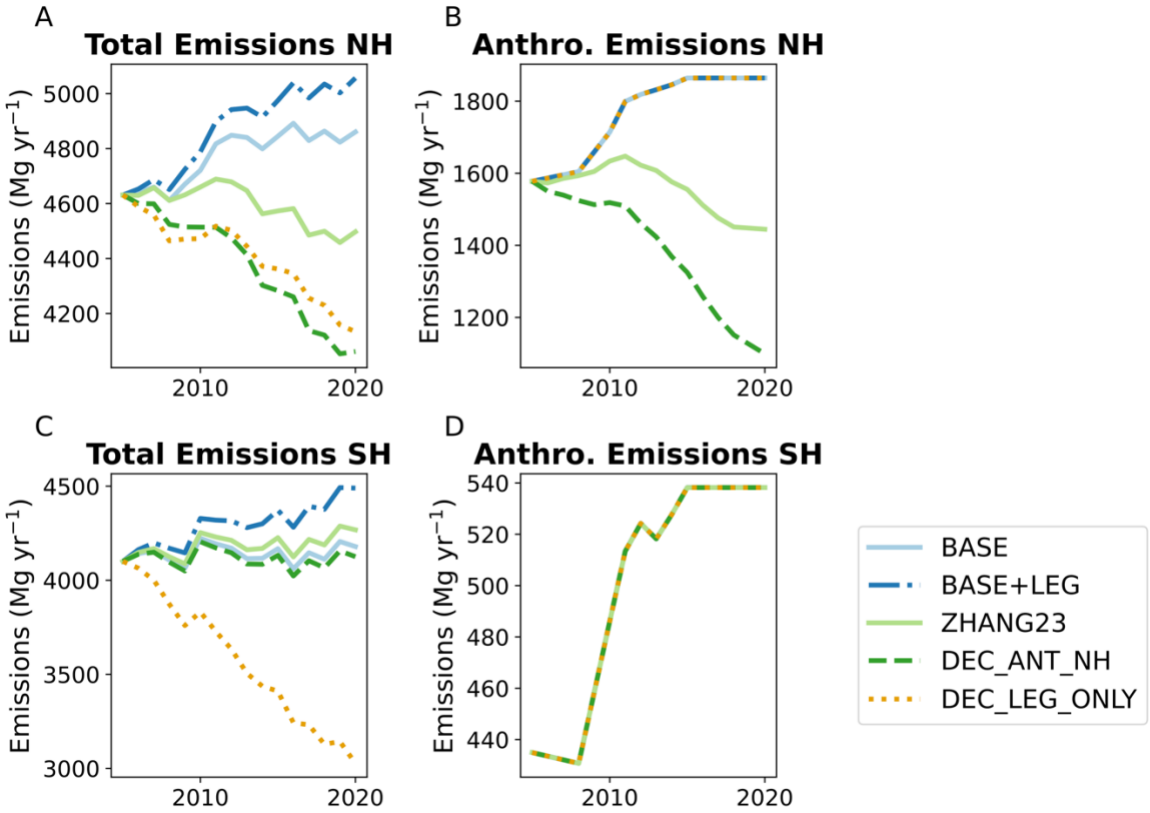

Figure S10. The emission timeseries in GEOS-Chem simulations for 2005–2020: total emissions in the Northern Hemisphere (*A*), anthropogenic emissions in the Northern Hemisphere (*B*), total emissions in the Southern Hemisphere (*C*), and anthropogenic emissions in the Southern Hemisphere (*D*).

Section S8. Dry deposition trend in GEOS-Chem simulations

The Leaf Area Index (LAI) data used in GEOS-Chem comes from a reprocessed version of the Moderate Resolution Imaging Spectroradiometer (MODIS) satellite product (32), and includes the observed interannual variations in vegetation. Our GEOS-Chem simulations thus include the impact of (LAI) variations during 2005–2020 on the dry deposition of Hg^0. The dry deposition scheme of GEOS-Chem and its response to changes in LAI have been thoroughly evaluated against observations by previous studies (33, 34). Here we evaluate the trends in the NH dry deposition of Hg^0 to investigate whether it is a major driver of the Hg^0 trends between 2005–2020.

Figure S11A shows the GEOS-Chem simulated fluxes of dry deposition over the BASE+LEG simulation. The dry deposition flux in the NH increases by 17 Mg yr^{-2} over the simulation, yet this is mainly due to the increasing emissions in the BASE+LEG scenario (+31 Mg yr^{-2} trend over simulation) increasing the amount of Hg^0 in the atmosphere. By dividing the NH Hg^0 burden by the dry deposition flux, we can calculate the dry deposition lifetime in the NH over the simulation (Fig. S11B). One observes a slight decline in the lifetime of Hg^0 dry deposition in the GEOS-Chem simulations over this time period, with a total decline in the lifetime of 3% between 2005 and 2020. Thus GEOS-Chem shows that the NH dry deposition of Hg^0 is indeed becoming faster over this time period, but not to the extent that it would reverse the emission driven changes in Hg^0 (Fig. 3C). Therefore, although it is important to further evaluate the impacts of changing vegetation on Hg cycling and its evolution in the future, during the 2005–2020 time period the dry deposition lifetime trends have a small impact compared to the estimated changes in anthropogenic Hg emissions.

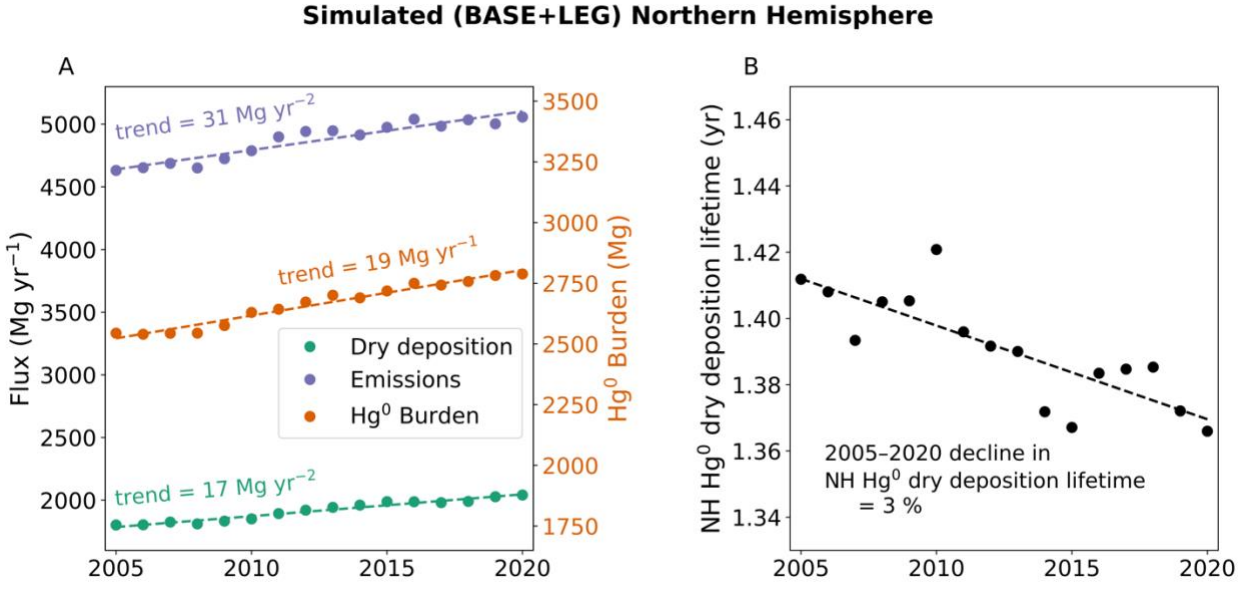

Figure S11. Impacts of changing vegetation on the dry deposition of Hg^0 in the NH. (*A*) Trends in the NH fluxes of dry deposition and total emissions in the BASE+LEG simulation (left y axis), along with changes in the NH Hg^0 burden (right y axis). Linear trend values are listed on the plot. (*B*) Trend in the Hg^0 NH dry deposition lifetime over the simulation, with the relative change between 2005 and 2020 listed on the plot.

Section S9. Additional quantile regression plots

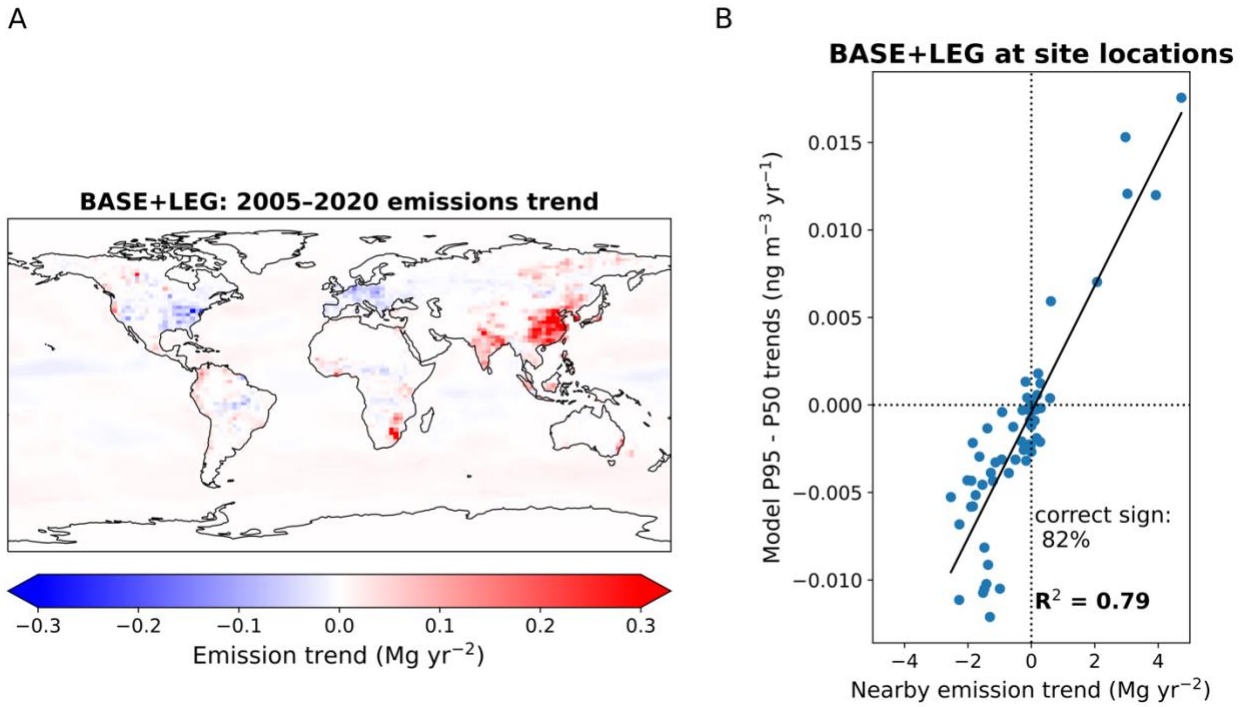

Figure S12. (*A*) Map of the linear trend of Hg emissions in the BASE+LEG simulation between 2005 and 2020. (*B*) Comparing the relationship between the BASE+LEG simulated nearby emission trend and the difference between the 95th percentile (P95) and median (P50) quantile regression Hg^0 trends at grid boxes corresponding to site locations (see Fig. 4C for the full P95 – P50 trends map). The nearby emission trend is calculated by summing emissions trends within two grid boxes (~500 km) of the site location grid box.

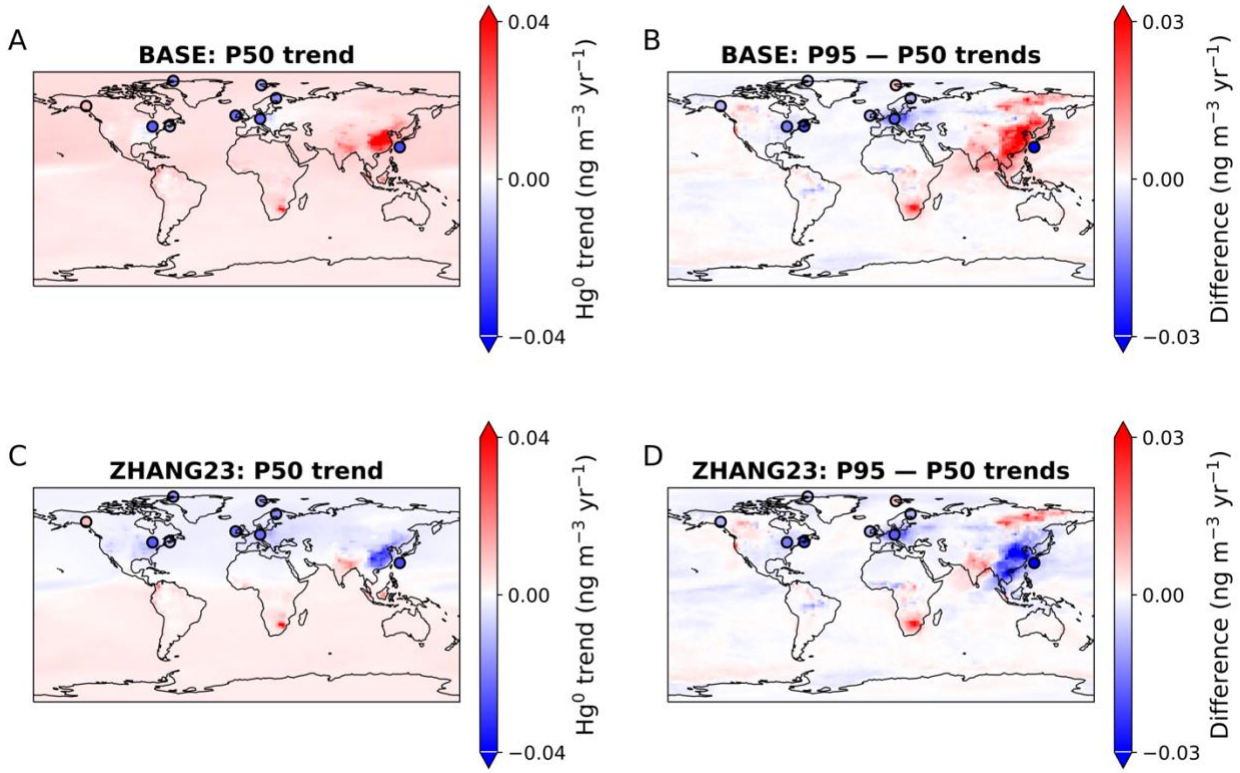

Figure S13. Trend in median (P50) daily deseasonalized simulated values in BASE (*A*) and ZHANG23 (*C*) for each model grid cell. Observed results are plotted in filled circles for 9 stations with more than 13 years of high frequency data. Differences between 95th percentile (P95) trend and median (P50) trend shown for BASE (*B*) and ZHANG23 (*D*) simulations and observations. The other simulations (BASE+LEG, DEC_ANT_NH, and DEC_LEG_ONLY) are shown in Fig. 4.

Section S10. Additional comparisons between observations and model simulations

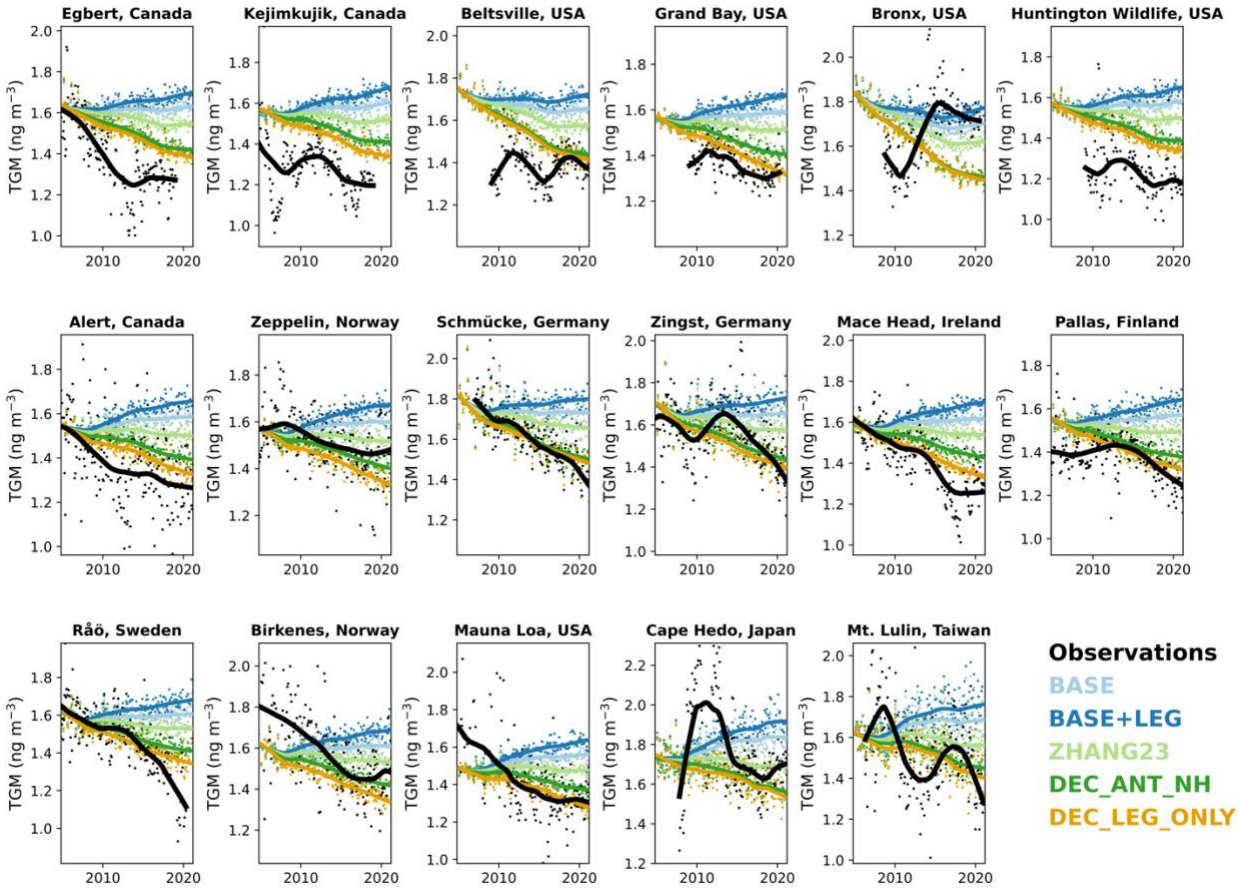

Figure S14. Timeseries plots comparing model simulations (colors) and observations (black) at stations with more than 12 years of data during 2005–2020. Markers show deseasonalized monthly means and lines show the smoothed tendency of the time series calculated using LOWESS (locally weighted scatterplot smoothing) regression.

Section S11. EDGAR v8.1_toxHg emissions inventory

A new anthropogenic emissions inventory has recently been released for 1970–2022, the EDGAR v8.1_toxHg inventory (35). Compared to the previous iteration of this inventory (EDGAR v4.tox2) (29), the v8.1 inventory includes updated spatial proxies and emissions factors and is extended to 2020. The released speciation maps (Hg^0, Hg^{2+}, Hg^P) from the inventory were still in draft form at the time of this manuscript, so we did not run GEOS-Chem simulations with v8.1_toxHg, though this will be upcoming in the MCHgMAP project (36). The total Hg emissions maps have been released in definitive form at this time, so we have analyzed the trends in the total emissions (Fig. S15). The NH trend between 2005 and 2020 is 35 Mg yr^{-2}, very similar to the Streets et al. (28) 2005–2015 trend (34 Mg yr^{-2}). Therefore, our modelling results using the Streets et al. (28) emissions trends are likely applicable to the new EDGAR v8.1_toxHg inventory as well. Increasing global and NH emissions are a common feature in both Streets et al. (28) and EDGAR v8.1_toxHg inventories, in contrast to the observed decline in Hg^0 concentrations.

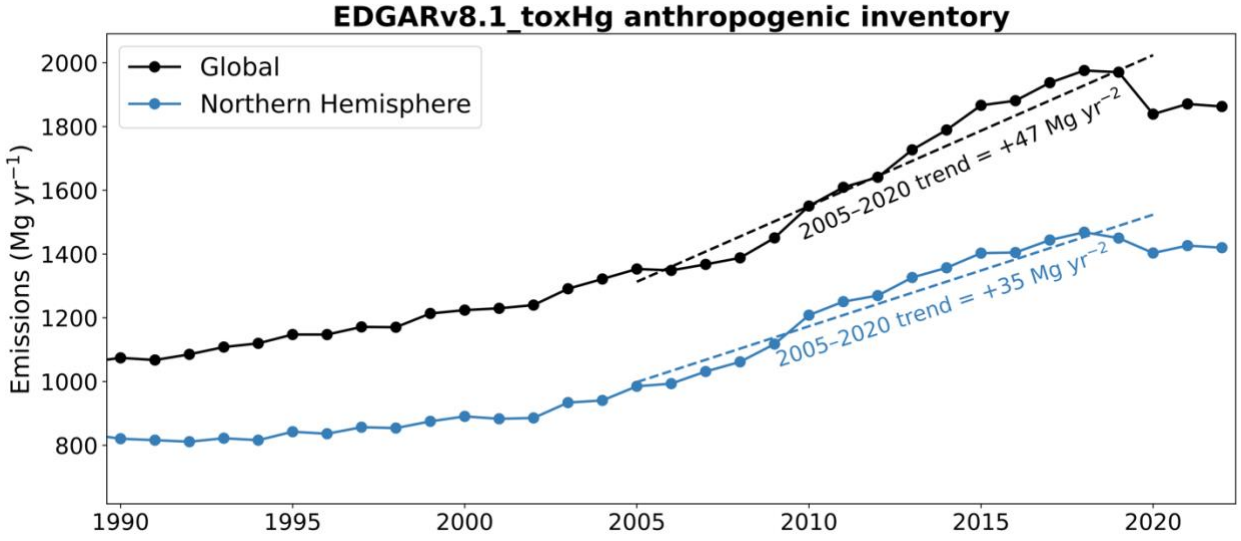

Figure S15. Anthropogenic emissions trend from the EDGARv8.1_tox anthropogenic inventory, with linear trends calculated and plotted for the 2005–2020 period.

Supplementary References

1. M. Iturbide, *et al.*, An update of IPCC climate reference regions for subcontinental analysis of climate model data: definition and aggregated datasets. *Earth Syst. Sci. Data* **12**, 2959–2970 (2020).
2. D. A. Gay, *et al.*, The Atmospheric Mercury Network: measurement and initial examination of an ongoing atmospheric mercury record across North America. *Atmos. Chem. Phys.* **13**, 11339–11349 (2013).
3. F. Carbone, *et al.*, Sea surface temperature variation linked to elemental mercury concentrations measured on Mauna Loa. *Geophys. Res. Lett.* **43**, 7751–7757 (2016).
4. F. Sprovieri, *et al.*, Atmospheric mercury concentrations observed at ground-based monitoring sites globally distributed in the framework of the GMOS network. *Atmos. Chem. Phys.* **16**, 11915–11935 (2016).
5. A. Cole, *et al.*, A Survey of Mercury in Air and Precipitation across Canada: Patterns and Trends. *Atmosphere* **5**, 635–668 (2014).
6. V. L. St. Louis, *et al.*, Atmospheric Concentrations and Wet/Dry Loadings of Mercury at the Remote Experimental Lakes Area, Northwestern Ontario, Canada. *Environ. Sci. Technol.* **53**, 8017–8026 (2019).

7. K. Tørseth, *et al.*, Introduction to the European Monitoring and Evaluation Programme (EMEP) and observed atmospheric composition change during 1972–2009. *Atmos. Chem. Phys.* **12**, 5447–5481 (2012).
8. L. S. P. Nguyen, G.-R. Sheu, D.-W. Lin, N.-H. Lin, Temporal changes in atmospheric mercury concentrations at a background mountain site downwind of the East Asia continent in 2006–2016. *Science of The Total Environment* **686**, 1049–1056 (2019).
9. K. Marumoto, *et al.*, Long-Term Observation of Atmospheric Speciated Mercury during 2007–2018 at Cape Hedo, Okinawa, Japan. *Atmosphere* **10**, 362 (2019).
10. Y. Zhang, *et al.*, Observed decrease in atmospheric mercury explained by global decline in anthropogenic emissions. *Proc. Natl. Acad. Sci. U.S.A.* **113**, 526–531 (2016).
11. K.-L. Chang, *et al.*, Trend detection of atmospheric time series. *Elementa: Science of the Anthropocene* **9**, 00035 (2021).
12. S. N. Wood, Fast stable restricted maximum likelihood and marginal likelihood estimation of semiparametric generalized linear models. *Journal of the Royal Statistical Society (B)* **73**, 3–36 (2011).
13. K.-L. Chang, M. G. Schultz, G. Koren, Selke, Niklas, Guidance note on best statistical practices for TOAR analyses. Available at: https://doi.org/10.48550/arXiv.2304.14236. (2023).
14. P. S. Weiss-Penzias, *et al.*, Trends in mercury wet deposition and mercury air concentrations across the U.S. and Canada. *Science of The Total Environment* **568**, 546–556 (2016).
15. M. S. Gustin, *et al.*, Measurement of Atmospheric Mercury: Current Limitations and Suggestions for Paths Forward. *Environ. Sci. Technol.* **58**, 12853–12864 (2024).
16. M. S. Gustin, *et al.*, Do We Understand What the Mercury Speciation Instruments Are Actually Measuring? Results of RAMIX. *Environ. Sci. Technol.* **47**, 7295–7306 (2013).
17. A. Steffen, *et al.*, A synthesis of atmospheric mercury depletion event chemistry in the atmosphere and snow. *Atmospheric Chemistry and Physics* **8**, 1445–1482 (2008).
18. K. MacSween, *et al.*, Updated trends for atmospheric mercury in the Arctic: 1995–2018. *Science of The Total Environment* **837**, 155802 (2022).
19. D. Custódio, *et al.*, Odds and ends of atmospheric mercury in Europe and over the North Atlantic Ocean: temporal trends of 25 years of measurements. *Atmos. Chem. Phys.* **22**, 3827–3840 (2022).
20. J. Gačnik, S. Lyman, S. M. Dunham-Cheatham, M. S. Gustin, Limitations and insights regarding atmospheric mercury sampling using gold. *Analytica Chimica Acta* **1319**, 342956 (2024).
21. N. E. Selin, A proposed global metric to aid mercury pollution policy. *Science* **360**, 607–609 (2018).
22. H. M. Amos, D. J. Jacob, D. G. Streets, E. M. Sunderland, Legacy impacts of all-time anthropogenic emissions on the global mercury cycle. *Global Biogeochem. Cycles* **27**, 410–421 (2013).
23. H. M. Amos, *et al.*, Global Biogeochemical Implications of Mercury Discharges from Rivers and Sediment Burial. *Environ. Sci. Technol.* **48**, 9514–9522 (2014).
24. M. D. McKay, R. J. Beckman, W. J. Conover, Comparison of Three Methods for Selecting Values of Input Variables in the Analysis of Output from a Computer Code. *Technometrics* **21**, 239–245 (1979).
25. H. M. Horowitz, *et al.*, A new mechanism for atmospheric mercury redox chemistry: implications for the global mercury budget. *Atmos. Chem. Phys.* **17**, 6353–6371 (2017).
26. J. P. Parrella, *et al.*, Tropospheric bromine chemistry: implications for present and pre-industrial ozone and mercury. *Atmos. Chem. Phys.* **12**, 6723–6740 (2012).
27. Y. Zhang, *et al.*, An updated global mercury budget from a coupled atmosphere-land-ocean model: 40% more re-emissions buffer the effect of primary emission reductions. *One Earth* **6**, 316–325 (2023).
28. D. G. Streets, *et al.*, Global and regional trends in mercury emissions and concentrations, 2010–2015. *Atmospheric Environment* **201**, 417–427 (2019).
29. M. Muntean, *et al.*, Evaluating EDGARv4.tox2 speciated mercury emissions ex-post scenarios and their impacts on modelled global and regional wet deposition patterns. *Atmospheric Environment* **184**, 56–68 (2018).
30. D. G. Streets, *et al.*, Five hundred years of anthropogenic mercury: spatial and temporal release profiles. *Environ. Res. Lett.* **14**, 084004 (2019).
31. H. Angot, *et al.*, Global and Local Impacts of Delayed Mercury Mitigation Efforts. *Environ. Sci. Technol.* **52**, 12968–12977 (2018).

32. H. Yuan, Y. Dai, Z. Xiao, D. Ji, W. Shangguan, Reprocessing the MODIS Leaf Area Index products for land surface and climate modelling. *Remote Sens. Environ.* **115**, 1171–1187 (2011).
33. A. Feinberg, T. Dlamini, M. Jiskra, V. Shah, N. E. Selin, Evaluating atmospheric mercury (Hg) uptake by vegetation in a chemistry-transport model. *Environ. Sci.: Processes Impacts* **24**, 1303–1318 (2022).
34. A. Feinberg, M. Jiskra, P. Borrelli, J. Biswakarma, N. E. Selin, Deforestation as an Anthropogenic Driver of Mercury Pollution. *Environ. Sci. Technol.* **58**, 3246–3257 (2024).
35. M. Muntean, *et al.*, EDGAR v8.1 Global Mercury Emissions. European Commission, Joint Research Centre (JRC) [Dataset] PID: http://data.europa.eu/89h/83b507d7-5218-4dc5-95f9-0ec36f073204. Deposited 2024.
36. A. Dastoor, *et al.*, The Multi-Compartment Hg Modeling and Analysis Project (MCHgMAP): Mercury modeling to support international environmental policy. *Geoscientific Model Development Discussions* **2024**, 1–171 (2024).